



PEARLS: A Potentially Isolated Quiescent Dwarf Galaxy with a Tip of the Red Giant Branch Distance of 30 Mpc

Timothy Carleton¹, Timothy Ellsworth-Bowers², Rogier A. Windhorst¹, Seth H. Cohen¹, Christopher J. Conselice³, Jose M. Diego⁴, Adi Zitrin⁵, Haylee N. Archer^{1,2}, Isabel McIntyre¹, Patrick Kamieneski¹, Rolf A. Jansen¹, Jake Summers¹, Jordan C. J. D’Silva^{6,7}, Anton M. Koekemoer⁸, Dan Coe^{8,9,10}, Simon P. Driver⁶, Brenda Frye¹¹, Norman A. Grogin⁸, Madeline A. Marshall^{7,12}, Mario Nonino¹³, Nor Pirzkal⁸, Aaron Robotham⁶, Russell E. Ryan, Jr.⁸, Rafael Ortiz III¹, Scott Tompkins⁶, Christopher N. A. Willmer¹¹, Haojing Yan¹⁴, and Benne W. Holwerda¹⁵

¹ School of Earth and Space Exploration, Arizona State University, Tempe, AZ 85287-1404, USA; tmcarlet@asu.edu

² Lowell Observatory, 1400 West Mars Hill Road, Flagstaff, AZ 86001, USA

³ Jodrell Bank Centre for Astrophysics, Alan Turing Building, University of Manchester, Oxford Road, Manchester M13 9PL, UK

⁴ Instituto de Física de Cantabria (CSIC-UC), Avenida. Los Castros s/n. E-39005 Santander, Spain

⁵ Physics Department, Ben-Gurion University of the Negev, P.O. Box 653, Beer-Sheva 84105, Israel

⁶ International Centre for Radio Astronomy Research (ICRAR) and the International Space Centre (ISC), The University of Western Australia, M468, 35 Stirling Highway, Crawley, WA 6009, Australia

⁷ ARC Centre of Excellence for All Sky Astrophysics in 3 Dimensions (ASTRO 3D), Australia

⁸ Space Telescope Science Institute, 3700 San Martin Drive, Baltimore, MD 21218, USA

⁹ Association of Universities for Research in Astronomy (AURA) for the European Space Agency (ESA), STScI, Baltimore, MD 21218, USA

¹⁰ Center for Astrophysical Sciences, Department of Physics and Astronomy, The Johns Hopkins University, 3400 N Charles Street, Baltimore, MD 21218, USA

¹¹ Steward Observatory, University of Arizona, 933 N Cherry Avenue, Tucson, AZ, 85721-0009, USA

¹² National Research Council of Canada, Herzberg Astronomy & Astrophysics Research Centre, 5071 West Saanich Road, Victoria, BC V9E 2E7, Canada

¹³ INAF-Osservatorio Astronomico di Trieste, Via Bazzoni 2, I-34124 Trieste, Italy

¹⁴ Department of Physics and Astronomy, University of Missouri, Columbia, MO 65211, USA

¹⁵ Department of Physics and Astronomy, University of Louisville, Louisville, KY 40292, USA

Received 2023 September 26; revised 2023 December 21; accepted 2023 December 28; published 2024 January 31

Abstract

A wealth of observations have long suggested that the vast majority of isolated classical dwarf galaxies ($M_* = 10^7\text{--}10^9 M_\odot$) are currently star forming. However, recent observations of the large abundance of “ultra-diffuse galaxies” beyond the reach of previous large spectroscopic surveys suggest that our understanding of the dwarf galaxy population may be incomplete. Here we report the serendipitous discovery of an isolated quiescent dwarf galaxy in the nearby Universe, which was imaged as part of the JWST PEARLS Guaranteed Time Observation program. Remarkably, individual red-giant branch stars are visible in this near-IR imaging, suggesting a distance of 30 ± 4 Mpc, and a wealth of archival photometry point to an sSFR of $2 \times 10^{-11} \text{ yr}^{-1}$ and star formation rate of $4 \times 10^{-4} M_\odot \text{ yr}^{-1}$. Spectra obtained with the Lowell Discovery Telescope find a recessional velocity consistent with the Hubble Flow and $>1500 \text{ km s}^{-1}$ separated from the nearest massive galaxy in Sloan Digital Sky Survey suggesting that this galaxy was either quenched from internal mechanisms or had a very high-velocity ($\gtrsim 1000 \text{ km s}^{-1}$) interaction with a nearby massive galaxy in the past. This analysis highlights the possibility that many nearby quiescent dwarf galaxies are waiting to be discovered and that JWST has the potential to resolve them.

Unified Astronomy Thesaurus concepts: Low surface brightness galaxies (940); James Webb Space Telescope (2291); Dwarf galaxies (416); Stellar populations (1622); Galaxy evolution (594)

1. Introduction

Our understanding of the process of star formation and quenching in classical dwarf galaxies remains poorly understood, despite the large number of detailed observations of local systems (Weisz et al. 2011; McConnachie 2012; Spekkens et al. 2014; Mao et al. 2021; Putman et al. 2021; Carlsten et al. 2022). This is partly due to the outsized influence of complex internal (e.g., star formation feedback; Dekel & Woo 2003; Hopkins et al. 2014; Agertz & Kravtsov 2016) and external (e.g., ram pressure stripping, galaxy harassment; Gunn & Gott 1972; Moore et al. 1996; Mayer et al. 2006; Boselli et al. 2008;

Fillingham et al. 2016; Wang et al. 2021; Wang et al. 2022) processes given their comparatively weak gravitational potential. These processes result in a large diversity in the star formation properties among the dwarf galaxy population (Weisz et al. 2011; de los Reyes & Kennicutt 2019).

Despite all the variation in dwarf galaxy properties, one constant seems to hold: isolated dwarf galaxies always seem to be star forming (Haines et al. 2007; Geha et al. 2012; Kawinwanichakij et al. 2017; Davies et al. 2019; Prole et al. 2021). Only a handful of objects are known to violate this rule (e.g., Karachentsev et al. 2015; Martínez-Delgado et al. 2016; Garling et al. 2020; Polzin et al. 2021; Casey et al. 2023), and most of these objects are just beyond massive groups or clusters for which they may have experienced some recent interaction. However, observations of a large number of “ultra-diffuse galaxies” in clusters (Koda et al. 2015; Mihos et al. 2015; Muñoz et al. 2015; van Dokkum et al. 2015; Román & Trujillo 2017a;



Original content from this work may be used under the terms of the [Creative Commons Attribution 4.0 licence](https://creativecommons.org/licenses/by/4.0/). Any further distribution of this work must maintain attribution to the author(s) and the title of the work, journal citation and DOI.

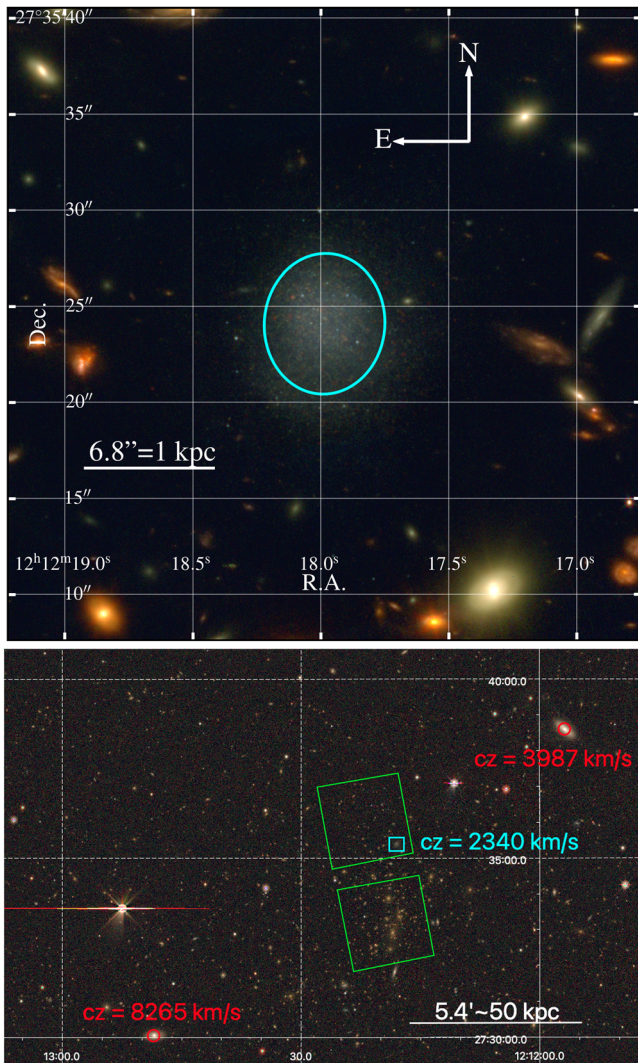


Figure 1. Top: the JWST of the PEARLSGD galaxy (blue = F090W + F150W, green = F200W + $0.5 \times$ F277W, red = $0.5 \times$ F277W + F356W + F444W). Bottom: DECALS *grz* image of the sky immediately surrounding PEARLSGD. Both images are aligned such that north is up and east is left. PEARLSGD is identified with the cyan box, and the green squares show the area covered by NIRC*am* imaging. Also shown are two of the closest (in-projection) nearby massive galaxies (identified in red circles).

Lee et al. 2020), groups (van der Burg et al. 2016), and the field (Román & Trujillo 2017b; Leisman et al. 2017; Prole et al. 2021), have led some to speculate that the star forming universality is hampered by selection effects and that many low-surface-brightness quiescent galaxies are waiting to be discovered (e.g., Román et al. 2019). Results from the SMUDGES survey (Zaritsky et al. 2019; Goto et al. 2023), which finds a statistical signature of quiescent ultra-diffuse galaxies well beyond the virial radii of massive hosts, give credence to this possibility.

Imaging with NIRC*am* (Rigby et al. 2023) on JWST has the potential to dramatically improve our understanding of nearby dwarf galaxy populations. Red giant branch (RGB) stars are approximately 2 mag brighter in the near-IR than optical wavelengths (McQuinn et al. 2017; Weisz et al. 2023), allowing for the possibility of measuring RGB distances beyond 30 Mpc and surface-brightness-fluctuation distances even further. This, in conjunction with the relative insensitivity of near-IR selected galaxies to age-based selection effects, means that a much more complete understanding of the

environment of dwarf galaxies, and the influence of that environment on the star formation of those galaxies, will soon be possible.

As a precursor to this potential wealth of discovery, we report the serendipitous discovery of an isolated, quiescent, classical dwarf galaxy at R.A. = $12^{\text{h}}12^{\text{m}}18^{\text{s}}$, decl. = $+27^{\circ}35^{\text{m}}24^{\text{s}}$, known as PEARLSGD throughout, in imaging of the CLG1212 cluster as part of the Prime Extragalactic Areas for Reionization and Lensing Science (PEARLS) program (Windhorst et al. 2023). While this galaxy has been photometrically identified in other surveys (DECaLS and Sloan Digital Sky Survey, SDSS), JWST imaging is able to resolve individual RGB stars constraining its distance to 30 ± 4 Mpc. Follow-up optical spectroscopy suggests that it is isolated from nearby massive galaxies, and spectral-energy-distribution fitting confirms that it is quiescent. Section 2 describes JWST and Lowell Discovery Telescope observations identifying the galaxy and measuring its recessional velocity. Section 3 describes the measurement of its basic properties, including its recessional velocity, point-source photometry of its stars, and aperture photometry of the whole object. Section 4 describes the inferred galaxy properties, including its distance measured with the tip of the red giant branch (TRGB) method (Section 4.1), its stellar population parameters, and star formation rate based on spectral-energy-distribution fitting (Section 4.3), and large-scale environment (Section 4.4). Finally, Section 5 summarizes our results and presents some preliminary interpretations. We utilize Vega magnitudes when discussing point-source stellar photometry and jansky when discussing aperture photometry. When applicable, we utilize a cosmology with $H_0 = 73 \text{ km s}^{-1} \text{ Mpc}^{-1}$ (Riess et al. 2022), $\Omega_m = 0.3$, and $\Omega_\Lambda = 0.7$.

2. Observations

Before its serendipitous observation as part of the PEARLS program, PEARLSGD had been photometrically identified in SDSS, DECaLS (Dey et al. 2019), Wide-field Infrared Survey Explorer (Wright et al. 2010), and GALEX surveys. It was also included in Spitzer IRAC 3.6, 4.5, 5.7, 8 μm , and MIPS 24 and 70 μm imaging of CLG1212¹⁶ (programs 20225, 13024; PI: Rines). For example, SDSS characterized it as an object with an *r*-band magnitude of 18.84, a half-light radius of $3''.6$, and an average surface brightness of $23.6 \text{ AB mag arcsec}^{-2}$. JWST F200W observations find similar structural parameters, with a best-fit Sérsic *n* of 0.8 and r_e of $3''.7$ (see Section 4.2). This ancillary imaging allows us to characterize the stellar populations of PEARLSGD in detail.

2.1. JWST Observations

The PEARLS program (Guaranteed Time Observation 1176; PI: Windhorst; Windhorst et al. 2023) targeted the CLG-J1212 +2733 cluster (Zitrin et al. 2020) on 2023 January 13–14. This field was observed with F090W, F150W, and F200W short-wavelength filters and F277W, F356W, and F444W long-wavelength filters. The median exposure times were 2491 s, 1890 s, and 1890 s for F090W, F150W, and F200W; and 1890 s, 1890 s, and 2491 s for F277W, F356W, and F444W. In the imaging, PEARLSGD appears in the non-cluster module,

¹⁶ It is just outside the footprint of the Hubble Space Telescope (HST) WFC3 and Advanced Camera for Surveys imaging of the cluster taken as part of GO: 15959; PI: Zitrin.

approximately $2\frac{1}{3}$ from the cluster. Figure 1(a) shows an RGB image of PEARLSDG using all JWST filters, and Figure 1(b) shows a DECaLS image of it and its surroundings.

The default PEARLS reductions described in Windhorst et al. (2023) apply ProFound-based sky subtractions (Robotham et al. 2017) and “wisp” removal (Robotham et al. 2023), which was designed to efficiently identify faint galaxies with small angular sizes. However, this affects low-surface-brightness features in PEARLSDG, so we use the standard STSCI reductions, which do not implement this sky subtraction. The JWST data are hosted at doi:10.17909/h26w-zh06, and will become publicly available 2024 January 13.

2.2. Lowell Discovery Telescope DeVeny Observations

Following the identification of this galaxy, it was observed with the DeVeny long-slit optical spectrograph on the Lowell Discovery Telescope. The observations were carried out on 2023 June 21, using a $1\frac{1}{5}$ -wide slit and the 5001/mm grating centered at $\lambda = 5000 \text{ \AA}$. Eleven exposures were taken, with a total of 1.3 hr spent on source. Much of the spectrum is affected by sinusoidal pattern noise that can affect the DeVeny camera.¹⁷ This sinusoidal noise was first subtracted by fitting the pattern noise across the slit.¹⁸ Following this correction, standard data reductions were completed using the PYPEIT software (Prochaska et al. 2020), which in addition to flat-field, bias, and wavelength calibrations, corrects for flexure effects using sky lines. The initial wavelength calibration was done using an ArI-CdI-Hg lamp, and sky lines were used to maintain the wavelength calibration throughout the night. The 2D spectra were stacked, weighting by the signal-to-noise ratio (S/N) of PEARLSDG, and a 1D spectrum was extracted using the optimal extraction procedure of Horne (1986).

3. Measurements

3.1. Point-source Photometry

We conduct point-source photometry on PEARLSDG using the DOLPHOT package (Dolphin 2000, 2016). Updates to the DOLPHOT software were implemented in 2023 April as part of the JWST Resolved Stellar Populations Early Release Science Program (Weisz et al. 2023). DOLPHOT uses point-spread functions (PSFs) created with WEBBPSF to iteratively subtract point sources identified in the image. Stars are identified in the combined I2D file and simultaneously fit to the F090W, F150W, and F200W CAL files. Aperture corrections are measured on isolated stars and applied to the measured fluxes. The parameters recommended for JWST observations in crowded fields¹⁹ (including $\text{img_apsky} = 20\ 35$, $\text{img_RAper} = 3$, and $\text{FitSky} = 2$) were adopted. The drizzled F200W image (where RGB stars are the brightest) was taken as the detection image, and photometry was conducted on all six JWST filters.

Similar to other works, (e.g., Dalcanton et al. 2009; Radburn-Smith et al. 2011; Danieli et al. 2020), we limit our selection to objects with the following DOLPHOT parameters: $\text{type} \leq 2$, $S/N_{F200W} > 4$, $S/N_{F150W} > 3$, $S/N_{F090W} > 3$, $\text{CROWD}_{F200W} < 0.3$, $\text{CROWD}_{F150W} < 0.3$, $\text{CROWD}_{F090W} < 0.3$, $|\text{sharp}|_{F200W} < 0.2$, $|\text{sharp}|_{F150W} < 0.2$, $|\text{sharp}|_{F090W} < 0.2$. We also exclude objects more than $8''$ from the galaxy center to reduce contamination from

background point sources like globular clusters. The criteria of $\text{CROWD} < 0.15$ largely restricts the sample to objects $> 1\frac{1}{5}$ from the center of the galaxy, so we do not apply any additional spatial cut.

Additionally, several (54) stars have unexpectedly red colors, with $F150W - F200W > 0.7$. The $F090W - F150W$ colors of these objects are expected, but due to their unusual $F150W - F200W$ colors, we exclude them from our sample. This leaves us with 94 stars. Figure 2(a) shows stars identified in the F200W image.

3.2. Recessional Velocity

As seen in Figure 3, the spectrum of PEARLSDG is relatively featureless and resembles a quiescent, low-mass galaxy. While the spectrum is just above the sky background, at least three spectral features can be identified in the stacked, smoothed spectrum: $H\gamma$ at $\sim 4370 \text{ \AA}$, $H\beta$ absorption at $\sim 4900 \text{ \AA}$, and Mg absorption at 5210 \AA . To measure the recessional velocity of PEARLSDG, we cross-correlate a model spectrum (constructed with PYTHON FSPS using a single stellar population of 10 Gyr and metallicity of -1.35) with the observed stacked spectrum. We exclude wavelengths below 4250 \AA given the low S/N. The best-fit redshift is $z = 0.0078$, corresponding to $2340 \pm 180 \text{ km s}^{-1}$. The largest source of uncertainty in this measurement comes from the use of a wide slit to obtain high enough S/N, so we assign a recessional velocity error based on moving the center of the object halfway across the slit (taken at $H\beta$). This corresponds to a recessional velocity error of 180 km s^{-1} .

3.3. Aperture Photometry

To fully understand the stellar population properties of PEARLSDG, we conduct aperture photometry on the existing UV-IR imaging and utilize archival imaging from GALEX, SDSS, DECaLS, JWST, and Spitzer. First, we use Source Extractor (Bertin & Arnouts 1996) to identify and mask nearby galaxies. We expand the mask around all objects by 2 pixels to ensure we mask as much flux from these nearby galaxies as possible. Then, we convolve all images to the $4\frac{1}{9}$ resolution of GALEX. The GALEX and Spitzer PSFs were obtained online,²⁰ the SDSS and DECaLS PSFs were modeled as Gaussians with FWHM noted in the catalog data, and the JWST PSFs were constructed from WEBBPSF v1.1.0. With these convolved images, we conduct aperture photometry using Python PHOTUTILS (Bradley et al. 2023). Based on trial and error, we find that aperture photometry with an $8''$ aperture minimizes the differences in measurements between different surveys and ensures we include nearly all the light from the galaxy in the convolved image. For JWST, we use a $10'' - 20''$ annulus (using the object-masked image) to estimate the background level; for SDSS and DECaLS, we utilize the existing background subtraction. For GALEX we use the published background maps for background subtraction, and for Spitzer, we use the Source Extractor background maps. No $24 \mu\text{m}$ emission is detected. Galactic extinction is corrected for using a Cardelli et al. (1989) extinction law assuming $E(B - V) = 0.019$ (Schlafly & Finkbeiner 2011). Note in Figure 1 that PEARLSDG is located in a sizeable NIRCcam area that is fortuitously devoid of brighter objects, making aperture

¹⁷ <http://www2.lowell.edu/users/tbowers/DevenyManualv171.pdf>

¹⁸ <https://github.com/LowellObservatory/LDObserverTools>

¹⁹ <http://americano.dolphinim.com/dolphot/dolphotNIRCcam.pdf>

²⁰ <http://www.galex.caltech.edu/researcher/techdoc-ch5.html> and <https://irsa.ipac.caltech.edu/data/SPITZER/docs/irac/calibrationfiles/psfprf/>

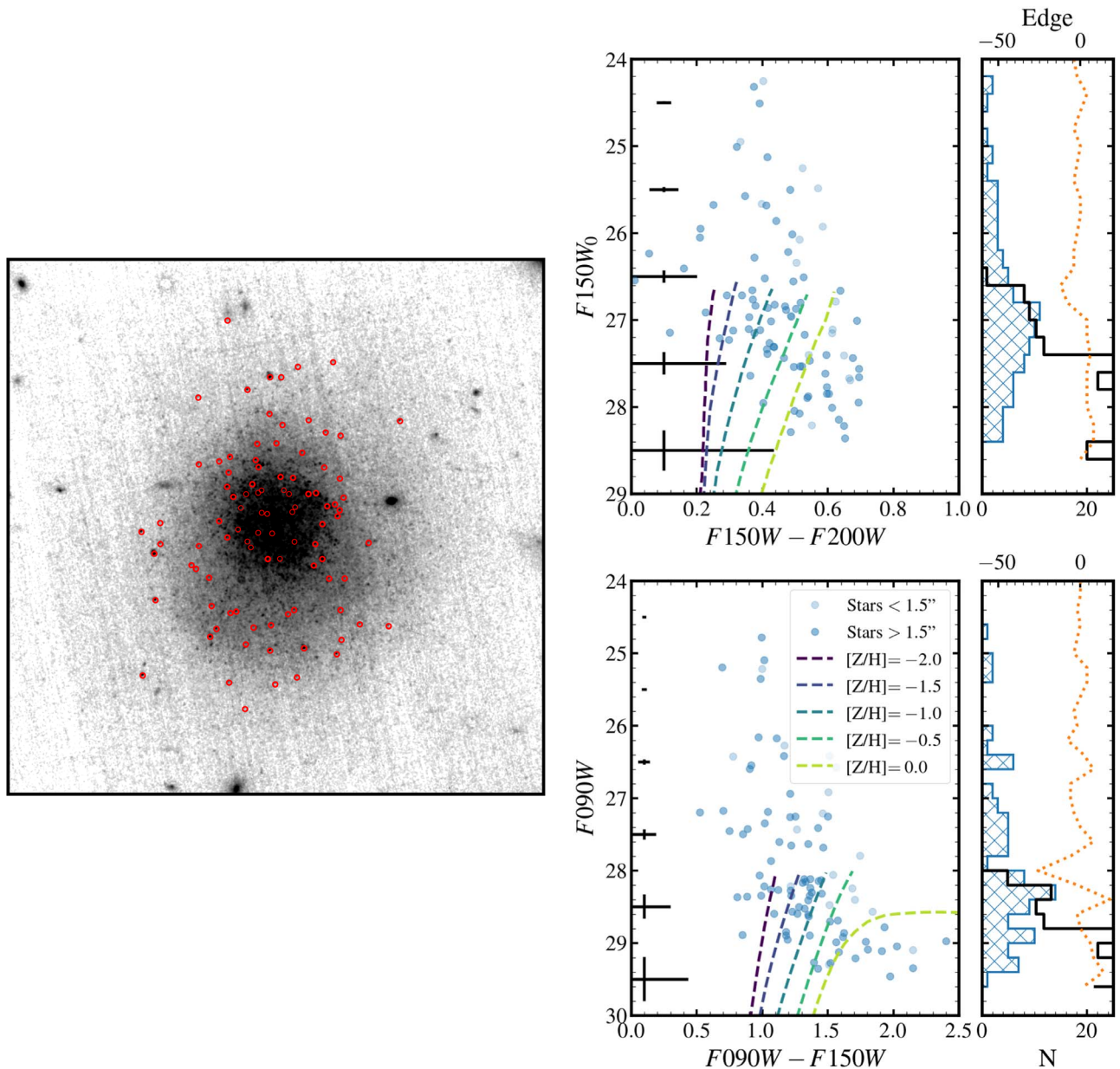


Figure 2. Left: F200W image of PEARLSGD with stars that pass our selection criteria circled in red (objects in the central $1.5''$ are thinner circles). While the imaging only pushes ~ 1 mag below the TRGB, a number of RGB stars are indeed visible. Right: color-magnitude diagrams for F150W–F200W (top) and F090W–F150W (bottom) point-source photometry, with F150W₀ and F090W luminosity functions (far right). Objects in the central $1.5''$ are shown as lighter points. The F150W–F200W color-magnitude diagram has been rectified (see Section 4.1). Average uncertainties as a function of magnitude are shown on the left. Also plotted are model 10 Gyr old RGB tracks of different metallicities (dashed lines) at a distance of 30.2 Mpc. A number of stars with colors and magnitudes consistent with the brightest RGB stars are visible with F150W–F200W colors of 0.2–0.7. While our imaging is not deep enough to identify the RGB in F090W as clearly as F150W₀, bright RGB stars identified in F150W₀ and F200W are clearly detected in F090W. This allows us to fit the F090W luminosity function to determine the RGB tip and distance modulus. The model luminosity function (shown as the black line) matches the characteristic jump in the observed F090W and rectified F150W luminosity functions. Lastly, the Sobel Filter response is shown as the orange dotted line. The strongest peak matches the TRGB in F090W and F150W₀. These results illustrate the promise of JWST to identify the TRGB in nearby galaxies.

photometry and sky subtraction possible in all these other images, which have much wider PSFs than JWST.

4. Results

4.1. TRGB Distance

The RGB “tip,” which represents the first He flash of a large number of old RGB stars, has been used extensively to measure distances to nearby galaxies using optical measurements with HST (e.g., Salaris & Cassisi 1997; Dalcanton et al. 2009, 2012;

Jang & Lee 2017a, 2017b; Freedman et al. 2019; McQuinn et al. 2019; Danieli et al. 2020; Freedman et al. 2020; Jang et al. 2020). The rectified F150W luminosity function shown Figure 2 shows a distinctive discontinuity associated with this TRGB. Notably, this RGB tip is about 2 mag brighter in the near-IR compared with *I*-band (McQuinn et al. 2019), allowing it to be more easily identified in JWST imaging. However, while the structure of the RGB and the absolute magnitude of the RGB tip have been shown to be insensitive to the parameters of the stellar population in the *I*-band, the same is

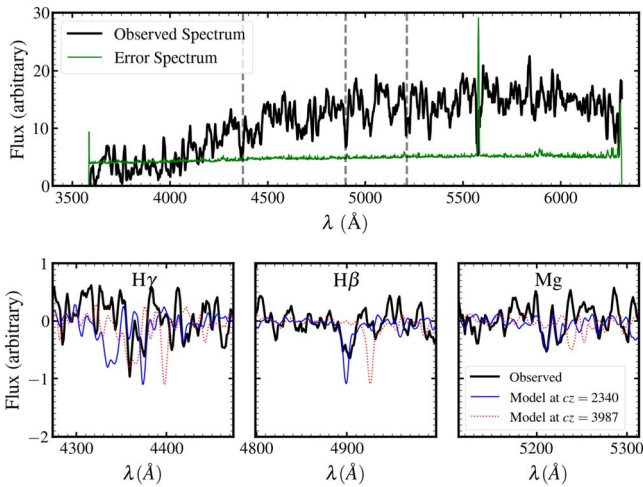


Figure 3. Top: observed spectrum (black) along with error spectrum (thin green line). Bottom: zoomed in on the $H\gamma$, $H\beta$, and Mg features (highlighted by dashed lines in the top panel). The model spectrum at the measured recession velocity of $cz = 2340 \pm 180 \text{ km s}^{-1}$ is shown as the thin blue line. For comparison, the red dotted line shows the model spectrum redshifted to the nearest massive galaxy at $cz = 3987 \text{ km s}^{-1}$. PEARLSGD is 1650 km s^{-1} separated from the nearest massive neighbor, so it is unlikely to be associated with it.

not necessarily true in the near-IR. The TRGB can vary by 0.75 mag depending on the assumed metallicity.

Given that the TRGB is flat in F090W, we do not rectify the F090W–F150W color–magnitude diagram. On the other hand, the TRGB is expected to (and does in our data) have a slope in F150W–F200W. The number of stars in PEARLSGD is not enough to independently rectify this TRGB, so we fit a line to the TRGB of PARSEC isochrones (Bressan et al. 2012; Marigo et al. 2013) with metallicities of -2.0 , -1.5 , -1.0 , -0.5 , and 0 , all with a 10 Gyr age to get the rectified F150W magnitude (which we refer to as F150W₀). We find a slope of -2.66 , and we normalize to the TRGB color of the -1.0 metallicity track of -0.392 .

To measure the TRGB distance, we take a forward-modeling approach following Danieli et al. (2020). Given the proven calibration of the I -band TRGB and its insensitivity to metallicity, we utilize the F090W luminosity function to fit the TRGB and use the rectified luminosity function as a check on this result. We generate an F090W luminosity function using the PARSEC isochrones (with the metallicity set to $Z/Z_{\odot} = 0.032$ and the age set to 10 Gyr) and a Kroupa (2001) initial mass function (IMF). Then, we model the observed luminosity function as a combination of this luminosity function and contaminants:

$$dN(m)/dm = dN_{\text{track}}(M + \mu)/dm + c_1(m - 27) + c_2, \quad (1)$$

where the first term represents the modeled stellar population (primarily the RGB, but including AGB stars as well) shifted to the assumed distance modulus (μ), and the second and third terms represent contamination (faint galaxies, pulsating AGB stars, foreground brown dwarfs, etc.). We optimize the likelihood of this model 100 times, varying the individual star measurements by their photometric uncertainties, to estimate the range of allowed parameters. We optimize the model over μ , c_1 , and c_2 , and find best-fit values of $\mu = 32.40 \pm 0.09$, $c_1 = 0.59 \pm 0.16$, and $c_2 = 1.36 \pm 0.2$.

This implies a distance of 30.2 Mpc, consistent with its Hubble distance of 32 ± 2.5 Mpc. Although the statistical uncertainty of this measurement represents a 1.1 Mpc uncertainty, we adopt a 0.3 mag, or 4 Mpc, uncertainty to account for other uncertainties (e.g., in the TRGB calibration). This measurement represents one of the most distant TRGB distance measurements to date (Freedman et al. 2020) and highlights the potential that JWST has to measure distances well beyond the local Universe. As a check on this modeling approach, we identify the TRGB by convolving the luminosity function with a Sobel filter ($[-2, 0, 2]$) for edge detection (shown as the orange lines in Figure 2). This finds an RGB tip at 28 mag in F090W, within 0.15 mag of the predicted TRGB at 30 Mpc in F090W from McQuinn et al. (2019). The tip of the rectified F150W₀ RGB is at 26.6 mag, also consistent with the prediction from McQuinn et al. (2019).

4.2. Structural Parameters

To independently estimate the structural parameters of PEARLSGD, we fit the light profile with GALFIT (Peng et al. 2002). We fit a single Sérsic component and one sky component to the I2D file downloaded from MAST. We include the derived parameters in Table 1. Notably, PEARLSGD has a low Sérsic index like many low-surface-brightness galaxies (e.g., Yagi et al. 2016).

4.3. SED Fitting

As apparent given the lack of emission lines in the optical spectra, PEARLSGD does not have a high current star formation rate. To fully understand its stellar population properties we model its stellar population with PROSPECTOR (Johnson et al. 2021), using the MILES stellar libraries (Sánchez-Blázquez et al. 2006; Falcón-Barroso et al. 2011), MIST isochrones (Choi et al. 2016; Dotter 2016), Draine & Li (2007) dust templates, and a Kroupa (2001) IMF. This model is fit to the aperture photometry described in Section 3.3. We adopt minimum uncertainties in the photometry of 1% to account for systematic errors such as zero-point differences (Rigby et al. 2023). The measured and best-fit spectral energy distribution is shown in Figure 4. Despite the blue JWST colors apparent in Figure 1, the optical spectrum is very red ($FUV - r > 3.4$), consistent with an old stellar population.

We model the star formation history as a five-component star formation history with t_{age}/yr bins at $[[0, 10^{7.5}], [10^{7.5}, 10^{8.5}], [10^{8.5}, 10^{9.5}], \text{ and } [10^{9.5}, 10^{10.11}]]$. In addition to modeling this star formation history, we fit for the dust content (simply modeled as a foreground screen with a power law with an index of -0.7 given its low star formation rate and low metallicity (Buzzo et al. 2022)). The results of our spectral energy distribution (SED) analysis are shown in Table 1. We find a best-fit metallicity of -1.32 and minimal dust extinction (τ_V , the dust opacity at 5500 has a best-fit value of 4.5×10^{-4}), consistent with its low mass and suggesting that it is not a tidal dwarf (e.g., Duc et al. 2001). Assuming the 30 Mpc distance derived in Section 4.1, we find a stellar mass of $1.7 \times 10^7 M_{\odot}$. The 90% upper limit on the fraction of the stellar population formed in the last $10^{8.5}$ yr is 0.3%, and the best-fit sSFR (SFR) within that time is $2.4 \times 10^{-11} \text{ yr}^{-1}$ ($4 \times 10^{-4} M_{\odot} \text{ yr}^{-1}$), with a 32 – 68 percentile range of $1.7 \times 10^{-12} - 1.4 \times 10^{-11} \text{ yr}^{-1}$ ($3 \times 10^{-5} - 2.8 \times 10^{-4} M_{\odot} \text{ yr}^{-1}$).

Table 1
Information about PEARLSDG

Parameter	Value
R.A.	12 ^h 12 ^m 18.0 ^s
decl.	+27 ^d 35 ^m 23.8 ^s
Distance	30 ± 4 Mpc
r_h	0.53 ± 0.70 kpc
b/a	0.85 ± 0.0007
Sérsic n	0.79 ± 0.0012
$f_{\text{Galax far ultraviolet (FUV)}}$	<4.18 μJy
$f_{\text{Galax near ultraviolet (NUV)}}$	<4.44 μJy
$f_{\text{SDSS } u}$	21 ± 5.0 μJy
$f_{\text{SDSS } g}$	55.8 ± 0.8 μJy
$f_{\text{SDSS } r}$	95.6 ± 0.9 μJy
$f_{\text{SDSS } i}$	96 ± 2.0 μJy
$f_{\text{DECALS } g}$	55.2 ± 0.8 μJy
$f_{\text{DECALS } r}$	91.2 ± 1.5 μJy
$f_{\text{DECALS } i}$	110 ± 1.9 μJy
$f_{\text{DECALS } z}$	123 ± 3.0 μJy
$f_{\text{JWST F090W}}$	125 ± 1.2 μJy
$f_{\text{JWST F150W}}$	156 ± 1.6 μJy
$f_{\text{JWST F200W}}$	140 ± 1.4 μJy
$f_{\text{JWST F277W}}$	72.6 ± 0.7 μJy
$f_{\text{JWST F356W}}$	48.9 ± 0.5 μJy
$f_{\text{JWST F444W}}$	34.1 ± 0.3 μJy
$f_{\text{Spitzer CH1}}$	48.1 ± 0.4 μJy
$f_{\text{Spitzer CH2}}$	28.9 ± 0.7 μJy
$f_{\text{Spitzer CH3}}$	15 ± 2 μJy
$f_{\text{Spitzer CH4}}$	<14 μJy
Current total M_*	$1.7 \pm 0.2 \times 10^7 M_\odot$
f_M^* formed log $t_{\text{age}}/\text{yr} \in [0,7.5]$	$1.6 \pm_1^5 \times 10^{-5}$
f_M^* formed log $t_{\text{age}}/\text{yr} \in [7.5,8.5]$	$5.2 \pm_5^{10} \times 10^{-4}$
f_M^* formed log $t_{\text{age}}/\text{yr} \in [8.5,9.7]$	$2.9 \pm_3^{30} \times 10^{-5}$
f_M^* formed log $t_{\text{age}}/\text{yr} \in [9.7,10]$	$9.2 \pm_9^{20} \times 10^{-5}$
f_M^* formed log $t_{\text{age}}/\text{yr} \in [10,10.11]$	0.997 ± 0.1
$\log(Z/Z_\odot)$	-1.35 ± 0.1
τ_V	$1.4 \pm_{0.79}^{0.94} \times 10^{-3}$

Note. The half-light radius (r_h), axis ratio (b/a) and Sérsic index (Sérsic n) are derived from Galfit modeling of the F200W image. Individual fluxes are calculated following the procedure of Section 3.3 with a minimum 1% uncertainty. The fraction of stellar mass formed in various age bins (f_M^*), metallicity (Z/Z_\odot), and dust opacity at 5500 Å (τ_V) are derived from Prospector SED fitting. The uncertainties are probably too small given possible systematic uncertainties, but it is clear that this galaxy is predominantly composed of an old, metal-poor stellar population.

Statistical uncertainties in the inferred SED parameters are quite low given the precise photometry across a wide wavelength range. Modeling uncertainties, such as the assumed IMF, stellar libraries, and detector zero-points are likely the limiting uncertainties. How these translate to uncertainties in the inferred model parameters (the star formation history parameters in particular) is difficult to say. Attempting to fit the SED with other model assumptions results in similar results. For example, fitting with a delayed- τ star formation history finds a very low τ value and old age ($\tau \sim 0.01$; $t_{\text{age}} \sim 10$ Gyr). This appears to be because the red near-IR colors (F090W through F200W) are only reproduced by a very old stellar population although fitting the SED without including the F200W or F150W photometry still results in a low sSFR. Regardless, to be conservative, we adopt a minimum 10% systematic uncertainty in the inferred SED parameters, following Conroy et al. (2009).

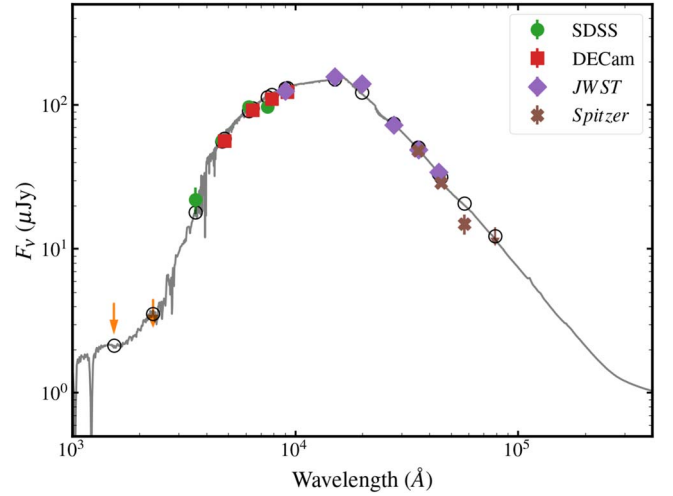


Figure 4. Broadband SED of PEARLSDG, including all available UV, optical, and near-IR data, shown alongside the best-fit SED from PROSPECTOR. The overlap of DECam and SDSS, as well as JWST and Spitzer bands, support the accuracy of our photometry. The SED is fit well with a predominantly old, metal-poor stellar population, with a very small contribution from younger stars.

The main uncertainty associated with the sSFR measurement is the amount of UV dust extinction. In our fiducial fitting, the low dust extinction is largely driven by the low Spitzer 5 and 8 micron fluxes although fitting with a polycyclic aromatic hydrocarbons fraction of 10^{-4} still arrives at a best fit with very little dust extinction. Allowing preferential dust extinction around young (10 Myr old) stars similarly finds a low sSFR of $1.2 \times 10^{-11} \text{ yr}^{-1}$.

Direct star formation rate estimates are not as constraining. The 3σ GALEX FUV luminosity is $4.8 \times 10^{24} \text{ erg s}^{-1} \text{ Hz}^{-1}$. Following the calibration of McQuinn et al. (2015), this results in an upper limit on the SFR of $9.8 \times 10^{-4} M_\odot \text{ yr}^{-1}$. Adopting 40% calibration uncertainty would put the limit at $1.4 \times 10^{-3} M_\odot \text{ yr}^{-1}$.

Regardless of the method used to estimate the SFR, we find that PEARLSDG has a remarkably low SFR. While constraints on the SFR- M_* relation are sparse in this mass range, Local Volume dwarfs from Lee et al. (2011) have sSFRs of $7 \times 10^{-11} \text{ yr}^{-1}$, above all but our most conservative sSFR limit and ~ 0.5 dex above our best estimate. Our best SFR estimate is 1.4 dex below the SFR- M_* relation of (Salim et al. 2007) when extrapolated to the stellar mass of PEARLSDG. Lastly, we compare PEARLSDG to objects in the NASA Sloan Atlas²¹ (NSA; Blanton et al. 2011). Of objects with a stellar mass within 0.3 dex within PEARLSDG, only 24% have a lower sSFR and 21% have a redder $FUV - r$ color.

4.4. Environment

To probe the environment of this galaxy, we draw from the NSA (Blanton et al. 2011). This catalog is optimized to analyze nearby galaxies in SDSS, such as PEARLSDG and its neighbors. We supplement this data with distance estimates from the CosmoFlows-4 catalog (Tully et al. 2023), containing direct distance estimates for a large number of local galaxies. Figure 5 shows PEARLSDG in the context of its surroundings, both in projected distance versus luminosity distance space

²¹ <http://www.nsatlas.org/>

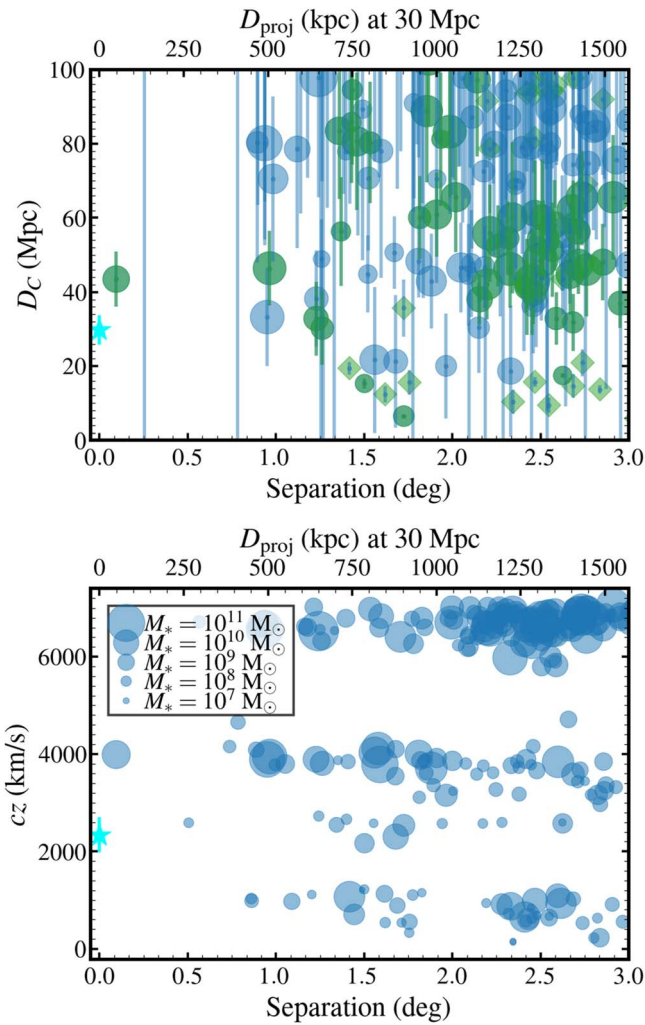


Figure 5. The large-scale environment of PEARLSDG. Both plots show the location of nearby galaxies with respect to PEARLSDG (shown as the cyan star), with point sizes proportional to the stellar mass of the system. Top: the co-moving distance to PEARLSDG from its TRGB, as a subset of objects in the NSA with either direct distance estimates from Cosmicflows-4 (green points) or our fundamental plane analysis (blue points). Objects in the Cosmicflows-4 catalog without a counterpart in the NSA are shown as light green diamonds defaulting to a stellar mass of $10^9 M_{\odot}$. Bottom: the recessional velocity of PEARLSDG and nearby systems in the NSA. PEARLSDG appears to be beyond the sphere of influence of any massive galaxy.

(using the fundamental plane, Cappellari et al. 2013, for galaxies besides PEARLSDG and those with direct distance estimates from Cosmicflows-4) and projected distance versus recessional velocity space (bottom). While PEARLSDG is the same general R.A., decl. coordinates of Virgo, Coma, and the Great Wall, it is actually in a very isolated region of space.

The closest massive galaxy (SDSS J121156.80+273835.5, or J1227) is 1650 km s^{-1} separated from PEARLSDG, and there are no massive ($>10^{10} M_{\odot}$) galaxies within 1000 km s^{-1} and 1 Mpc, making it one of the most isolated quiescent dwarf galaxies observed. This is further demonstrated in the top panel of Figure 5; the CosmicFlows-4 distance to J1227 is $43.5 \pm 7 \text{ Mpc}$, 1.9σ away from PEARLSDG. This is in agreement with the flow-model distance from Cosmicflows-4²² (Kourkchi et al. 2020), and would require a $+1797 \text{ km s}^{-1}$

peculiar velocity to be nearby in a region of space where the typical peculiar velocity is -195 km s^{-1} , further suggesting that PEARLSDG and J1227 are indeed not physically associated.

Regardless, we cannot completely rule out past interactions with other galaxies that may have affected its formation history. For example, it is possible it had a high-speed interaction with J1227 recently, and was quenched by that flyby interaction (Benavides et al. 2021). Alternatively, perhaps it interacted with nearby low-mass galaxies or a cosmic sheet and was quenched through that interaction (Garling et al. 2020; Pasha et al. 2023). However, the recessional velocity and luminosity distance of PEARLSDG are consistent with it being in the Hubble Flow, and there are no visible signatures of tidal interactions (see Figure 1).

5. Discussion

In this paper, we have reported the serendipitous discovery of PEARLSDG: a dwarf galaxy in PEARLS imaging of the CLG1212 field. This deep JWST imaging allows us to resolve individual RGB stars in this object and characterize its distance as $30 \pm 4 \text{ Mpc}$. This represents one of the farthest objects for which a TRGB distance has been determined and highlights the potential for JWST to measure distances to galaxies in the nearby Universe.

By combining PEARLS imaging with existing UV-IR imaging, we are able to constrain the stellar population properties of PEARLSDG. Consistent with its low level of UV emission and the lack of emission lines in its spectrum, we find a very low sSFR, suggesting that its star formation shut off over 1 Gyr ago. Deeper follow-up spectroscopy is necessary to understand its formation history and abundance patterns in detail.

Most models for quenching dwarf galaxies have focused on environmental effects (Bahé & McCarthy 2015; Alberts & Noble 2022) such as ram pressure stripping (e.g., Gunn & Gott 1972; Bekki 2009; Fillingham et al. 2016; Boselli et al. 2022), strangulation (Larson et al. 1980; Kawata & Mulchaey 2008), or tidal stripping (Moore et al. 1996). However, recent observations of large numbers of ultra-diffuse galaxies have prompted the development of internal quenching mechanisms, such as strong feedback (Mori et al. 2002). More unusual environmental effects such as flyby quenching, in which a quenched galaxy is ejected from the host after a high-speed interaction, have also been proposed (Benavides et al. 2021). More detailed analysis of the star formation history of PEARLSDG and the dynamics of PEARLSDG with respect to its surroundings are needed to further understand its formation history, but this discovery suggests the possibility that many isolated quiescent galaxies are waiting to be identified and that JWST has the tools to do so.

Acknowledgments

This work is based on observations made with the NASA/ESA/CSA James Webb Space Telescope. The data were obtained from the Mikulski Archive for Space Telescopes (MAST) at the Space Telescope Science Institute, which is operated by the Association of Universities for Research in Astronomy, Inc., under NASA contract NAS 5-03127 for JWST. These observations are associated with JWST programs 1176 and 2738.

²² <https://edd.ifa.hawaii.edu/CF4calculator/>










T.M.C. is grateful for support from the Beus Center for Cosmic Foundations. R.A.W., S.H.C., and R.A.J. acknowledge support from NASA JWST Interdisciplinary Scientist grants NAG5-12460, NNX14AN10G and 80NSSC18K0200 from GSFC. J.M.D. acknowledges the support of project PGC2018-101814-B-100 (MCIU/AEI/MINECO/FEDER, UE) Ministerio de Ciencia, Investigación y Universidades. This project was funded by the Agencia Estatal de Investigación, Unidad de Excelencia María de Maeztu, ref. MDM-2017-0765. C.C. is supported by the National Natural Science Foundation of China, Nos. 11803044, 11933003, 12173045. This work is sponsored (in part) by the Chinese Academy of Sciences (CAS), through a grant to the CAS South America Center for Astronomy (CASSACA). We acknowledge the science research grants from the China Manned Space Project with No. CMS-CSST-2021-A05. R.A.B. gratefully acknowledges support from the European Space Agency (ESA) Research Fellowship. C.J.C. acknowledges support from the European Research Council (ERC) Advanced Investigator Grant EPOCHS (788113). C.N.A.W. acknowledges funding from the JWST/NIRCam contract NASS-0215 to the University of Arizona. M.A.M. acknowledges the support of a National Research Council of Canada Plaskett Fellowship, and the Australian Research Council Centre of Excellence for All Sky Astrophysics in 3 Dimensions (ASTRO 3D), through project number CE17010001.

We also acknowledge the indigenous peoples of Arizona, including the Akimel O'odham (Pima) and Pee Posh (Maricopa) Indian Communities, whose care and keeping of the land has enabled us to be at ASU's Tempe campus in the Salt River Valley, where much of our work was conducted. Lowell Observatory sits at the base of mountains sacred to tribes throughout the region. We honor their past, present, and future generations, who have lived here for millennia and will forever call this place home.

Facility: JWST; Mikulski Archive <https://archive.stsci.edu>; Lowell Discovery Telescope.

Software: Astropy: <http://www.astropy.org> (Astropy Collaboration et al. 2018; Robitaille et al. 2021; Photutils: <https://photutils.readthedocs.io/en/stable/> (Bradley et al. 2020); ProFound: <https://github.com/asgr/ProFound> (Robotham et al. 2017, 2018); ProFit: <https://github.com/ICRAR/ProFit> (Robotham et al. 2018); SourceExtractor: <https://sextractor.readthedocs.io/en/latest/> (Bertin & Arnouts 1996); Python FSPS: <https://dfm.io/python-fsps/current/> (Conroy et al. 2009, 2010; Foreman-Mackey et al. 2014); Prospector: <https://prospect.readthedocs.io/en/latest/> (Johnson et al. 2021); WebbPSF: <https://webbpsf.readthedocs.io/en/latest/>.

ORCID iDs

Timothy Carleton  <https://orcid.org/0000-0001-6650-2853>
 Timothy Ellsworth-Bowers  <https://orcid.org/0000-0001-5695-7002>
 Rogier A. Windhorst  <https://orcid.org/0000-0001-8156-6281>
 Seth H. Cohen  <https://orcid.org/0000-0003-3329-1337>
 Christopher J. Conselice  <https://orcid.org/0000-0003-1949-7638>
 Jose M. Diego  <https://orcid.org/0000-0001-9065-3926>
 Adi Zitrin  <https://orcid.org/0000-0002-0350-4488>
 Haylee N. Archer  <https://orcid.org/0000-0002-8449-4815>
 Isabel McIntyre  <https://orcid.org/0000-0003-0230-6153>

Patrick Kamieneski  <https://orcid.org/0000-0001-9394-6732>
 Rolf A. Jansen  <https://orcid.org/0000-0003-1268-5230>
 Jake Summers  <https://orcid.org/0000-0002-7265-7920>
 Jordan C. J. D'Silva  <https://orcid.org/0000-0002-9816-1931>
 Anton M. Koekemoer  <https://orcid.org/0000-0002-6610-2048>
 Dan Coe  <https://orcid.org/0000-0001-7410-7669>
 Simon P. Driver  <https://orcid.org/0000-0001-9491-7327>
 Brenda Frye  <https://orcid.org/0000-0003-1625-8009>
 Norman A. Grogin  <https://orcid.org/0000-0001-9440-8872>
 Madeline A. Marshall  <https://orcid.org/0000-0001-6434-7845>
 Mario Nonino  <https://orcid.org/0000-0001-6342-9662>
 Nor Pirzkal  <https://orcid.org/0000-0003-3382-5941>
 Aaron Robotham  <https://orcid.org/0000-0003-0429-3579>
 Russell E. Ryan, Jr.  <https://orcid.org/0000-0003-0894-1588>
 Rafael Ortiz III  <https://orcid.org/0000-0002-6150-833X>
 Scott Tompkins  <https://orcid.org/0000-0001-9052-9837>
 Christopher N. A. Willmer  <https://orcid.org/0000-0001-9262-9997>
 Haojing Yan  <https://orcid.org/0000-0001-7592-7714>
 Benne W. Holwerda  <https://orcid.org/0000-0002-4884-6756>

References

- Agertz, O., & Kravtsov, A. V. 2016, *ApJ*, 824, 79
 Alberts, S., & Noble, A. 2022, *Univ*, 8, 554
 Astropy Collaboration, Price-Whelan, A. M., Sipőcz, B. M., et al. 2018, *AJ*, 156, 123
 Bahé, Y. M., & McCarthy, I. G. 2015, *MNRAS*, 447, 969
 Bekki, K. 2009, *MNRAS*, 399, 2221
 Benavides, J. A., Sales, L. V., Abadi, M. G., et al. 2021, *NatAs*, 5, 1255
 Bertin, E., & Arnouts, S. 1996, *A&AS*, 117, 393
 Blanton, M. R., Kazin, E., Muna, D., Weaver, B. A., & Price-Whelan, A. 2011, *AJ*, 142, 31
 Boselli, A., Boissier, S., Cortese, L., & Gavazzi, G. 2008, *ApJ*, 674, 742
 Boselli, A., Fossati, M., & Sun, M. 2022, *A&ARv*, 30, 3
 Bradley, L., Sipőcz, B., Robitaille, T., et al. 2020, *astropy/photutils: v1.0.1*, Zenodo, doi:10.5281/zenodo.4049061
 Bradley, L., Sipőcz, B., Robitaille, T., et al. 2023, *astropy/photutils: v1.8.0*, Zenodo, doi:10.5281/zenodo.7946442
 Bressan, A., Marigo, P., Girardi, L., et al. 2012, *MNRAS*, 427, 127
 Buzzo, M. L., Forbes, D. A., Brodie, J. P., et al. 2022, *MNRAS*, 517, 2231
 Cappellari, M., Scott, N., Alatalo, K., et al. 2013, *MNRAS*, 432, 1709
 Cardelli, J. A., Clayton, G. C., & Mathis, J. S. 1989, *ApJ*, 345, 245
 Carlsten, S. G., Greene, J. E., Beaton, R. L., Danieli, S., & Greco, J. P. 2022, *ApJ*, 933, 47
 Casey, K. J., Greco, J. P., Peter, A. H. G., & Davis, A. B. 2023, *MNRAS*, 520, 4715
 Choi, J., Dotter, A., Conroy, C., et al. 2016, *ApJ*, 823, 102
 Conroy, C., Gunn, J. E., & White, M. 2009, *ApJ*, 699, 486
 Conroy, C., White, M., & Gunn, J. E. 2010, *ApJ*, 708, 58
 Dalcanton, J. J., Williams, B. F., Melbourne, J. L., et al. 2012, *ApJS*, 198, 6
 Dalcanton, J. J., Williams, B. F., Seth, A. C., et al. 2009, *ApJS*, 183, 67
 Danieli, S., van Dokkum, P., Abraham, R., et al. 2020, *ApJL*, 895, L4
 Davies, L. J. M., Robotham, A. S. G., Lagos, C. d. P., et al. 2019, *MNRAS*, 483, 5444
 de los Reyes, M. A. C., & Kennicutt, Robert C. J. 2019, *ApJ*, 872, 16
 Dekel, A., & Woo, J. 2003, *MNRAS*, 344, 1131
 Dey, A., Schlegel, D. J., Lang, D., et al. 2019, *AJ*, 157, 168
 Dolphin, A., 2016 DOLPHOT: Stellar photometry, Astrophysics Source Code Library, ascl:1608.013
 Dolphin, A. E. 2000, *PASP*, 112, 1383
 Dotter, A. 2016, *ApJS*, 222, 8
 Draine, B. T., & Li, A. 2007, *ApJ*, 657, 810
 Duc, P. A., Cayatte, V., Balkowski, C., et al. 2001, *A&A*, 369, 763
 Falcón-Barroso, J., Sánchez-Blázquez, P., Vazdekis, A., et al. 2011, *A&A*, 532, A95
 Fillingham, S. P., Cooper, M. C., Pace, A. B., et al. 2016, *MNRAS*, 463, 1916

- Foreman-Mackey, D., Sick, J., & Johnson, B. 2014, [python-fsps: Python bindings to FSPP, v0.1.1](#), Zenodo, doi:10.5281/zenodo.12157
- Freedman, W. L., Madore, B. F., Hatt, D., et al. 2019, [ApJ](#), **882**, 34
- Freedman, W. L., Madore, B. F., Hoyt, T., et al. 2020, [ApJ](#), **891**, 57
- Garling, C. T., Peter, A. H. G., Kochanek, C. S., Sand, D. J., & Crnojević, D. 2020, [MNRAS](#), **492**, 1713
- Geha, M., Blanton, M. R., Yan, R., & Tinker, J. L. 2012, [ApJ](#), **757**, 85
- Goto, H., Zaritsky, D., Karunakaran, A., Donnerstein, R., & Sand, D. J. 2023, [AJ](#), **166**, 185
- Gunn, J. E., & Gott, J. R. I. 1972, [ApJ](#), **176**, 1
- Haines, C. P., Gargiulo, A., La Barbera, F., et al. 2007, [MNRAS](#), **381**, 7
- Hopkins, P. F., Kereš, D., Oñorbe, J., et al. 2014, [MNRAS](#), **445**, 581
- Horne, K. 1986, [PASP](#), **98**, 609
- Jang, I. S., de Jong, R. S., Holwerda, B. W., et al. 2020, [A&A](#), **637**, A8
- Jang, I. S., & Lee, M. G. 2017a, [ApJ](#), **835**, 28
- Jang, I. S., & Lee, M. G. 2017b, [ApJ](#), **836**, 74
- Johnson, B. D., Leja, J., Conroy, C., & Speagle, J. S. 2021, [ApJS](#), **254**, 22
- Karachentsev, I. D., Kniazev, A. Y., & Sharina, M. E. 2015, [AN](#), **336**, 707
- Kawata, D., & Mulchaey, J. S. 2008, [ApJL](#), **672**, L103
- Kawinwanichakij, L., Papovich, C., Quadri, R. F., et al. 2017, [ApJ](#), **847**, 134
- Koda, J., Yagi, M., Yamanoi, H., & Komiyama, Y. 2015, [ApJL](#), **807**, L2
- Kourkchi, E., Courtois, H. M., Graziani, R., et al. 2020, [AJ](#), **159**, 67
- Kroupa, P. 2001, [MNRAS](#), **322**, 231
- Larson, R. B., Tinsley, B. M., & Caldwell, C. N. 1980, [ApJ](#), **237**, 692
- Lee, J. C., Gil de Paz, A., Kennicutt, R. C. J., et al. 2011, [ApJS](#), **192**, 6
- Lee, J. H., Kang, J., Lee, M. G., & Jang, I. S. 2020, [ApJ](#), **894**, 75
- Leisman, L., Haynes, M. P., Janowiecki, S., et al. 2017, [ApJ](#), **842**, 133
- Mao, Y.-Y., Geha, M., Wechsler, R. H., et al. 2021, [ApJ](#), **907**, 85
- Marigo, P., Bressan, A., Nanni, A., Girardi, L., & Pumo, M. L. 2013, [MNRAS](#), **434**, 488
- Martínez-Delgado, D., Läsker, R., Sharina, M., et al. 2016, [AJ](#), **151**, 96
- Mayer, L., Mastrogiro, C., Wadsley, J., Stadel, J., & Moore, B. 2006, [MNRAS](#), **369**, 1021
- McConnachie, A. W. 2012, [AJ](#), **144**, 4
- McQuinn, K. B. W., Boyer, M., Skillman, E. D., & Dolphin, A. E. 2019, [ApJ](#), **880**, 63
- McQuinn, K. B. W., Boyer, M. L., Mitchell, M. B., et al. 2017, [ApJ](#), **834**, 78
- McQuinn, K. B. W., Skillman, E. D., Dolphin, A. E., & Mitchell, N. P. 2015, [ApJ](#), **808**, 109
- Mihos, J. C., Durrell, P. R., Ferrarese, L., et al. 2015, [ApJL](#), **809**, L21
- Moore, B., Katz, N., Lake, G., Dressler, A., & Oemler, A. 1996, [Natur](#), **379**, 613
- Mori, M., Ferrara, A., & Madau, P. 2002, [ApJ](#), **571**, 40
- Muñoz, R. P., Eigenthaler, P., Puzia, T. H., et al. 2015, [ApJL](#), **813**, L15
- Pasha, I., Mandelker, N., van den Bosch, F. C., Springel, V., & van de Voort, F. 2023, [MNRAS](#), **520**, 2692
- Peng, C. Y., Ho, L. C., Impey, C. D., & Rix, H.-W. 2002, [AJ](#), **124**, 266
- Polzin, A., van Dokkum, P., Danieli, S., Greco, J. P., & Romanowsky, A. J. 2021, [ApJL](#), **914**, L23
- Prochaska, J., Hennawi, J., Westfall, K., et al. 2020, [JOSS](#), **5**, 2308
- Prole, D. J., van der Burg, R. F. J., Hilker, M., & Spitler, L. R. 2021, [MNRAS](#), **500**, 2049
- Putman, M. E., Zheng, Y., Price-Whelan, A. M., et al. 2021, [ApJ](#), **913**, 53
- Radburn-Smith, D. J., de Jong, R. S., Seth, A. C., et al. 2011, [ApJS](#), **195**, 18
- Riess, A. G., Yuan, W., Macri, L. M., et al. 2022, [ApJL](#), **934**, L7
- Rigby, J., Perrin, M., McElwain, M., et al. 2023, [PASP](#), **135**, 048001
- Robitaille, T., Tollerud, E., Aldcroft, T., et al. 2021, [astropy/astropy: v4.2.1](#), Zenodo, doi:10.5281/zenodo.4670729
- Robotham, A. S. G., Davies, L. J. M., Driver, S. P., et al. 2018, [MNRAS](#), **476**, 3137
- Robotham, A. S. G., D'Silva, J. C. J., Windhorst, R. A., et al. 2023, [PASP](#), **135**, 085003
- Robotham, A. S. G., Taranu, D. S., Tobar, R., Moffett, A., & Driver, S. P. 2017, [MNRAS](#), **466**, 1513
- Román, J., Beasley, M. A., Ruiz-Lara, T., & Valls-Gabaud, D. 2019, [MNRAS](#), **486**, 823
- Román, J., & Trujillo, I. 2017a, [MNRAS](#), **468**, 703
- Román, J., & Trujillo, I. 2017b, [MNRAS](#), **468**, 4039
- Salaris, M., & Cassisi, S. 1997, [MNRAS](#), **289**, 406
- Salim, S., Rich, R. M., Charlot, S., et al. 2007, [ApJS](#), **173**, 267
- Sánchez-Blázquez, P., Peletier, R. F., Jiménez-Vicente, J., et al. 2006, [MNRAS](#), **371**, 703
- Schlafly, E. F., & Finkbeiner, D. P. 2011, [ApJ](#), **737**, 103
- Spekkens, K., Urbancic, N., Mason, B. S., Willman, B., & Aguirre, J. E. 2014, [ApJL](#), **795**, L5
- Tully, R. B., Kourkchi, E., Courtois, H. M., et al. 2023, [ApJ](#), **944**, 94
- van der Burg, R. F. J., Muzzin, A., & Hoekstra, H. 2016, [A&A](#), **590**, A20
- van Dokkum, P. G., Abraham, R., Merritt, A., et al. 2015, [ApJL](#), **798**, L45
- Wang, J., Staveley-Smith, L., Westmeier, T., et al. 2021, [ApJ](#), **915**, 70
- Wang, S., Wang, J., For, B.-Q., et al. 2022, [ApJ](#), **927**, 66
- Weisz, D. R., Dalcanton, J. J., Williams, B. F., et al. 2011, [ApJ](#), **739**, 5
- Weisz, D. R., McQuinn, K. B. W., Savino, A., et al. 2023, [ApJS](#), **268**, 15
- Windhorst, R. A., Cohen, S. H., Jansen, R. A., et al. 2023, [AJ](#), **165**, 13
- Wright, E. L., Eisenhardt, P. R. M., Mainzer, A. K., et al. 2010, [AJ](#), **140**, 1868
- Yagi, M., Koda, J., Komiyama, Y., & Yamanoi, H. 2016, [ApJS](#), **225**, 11
- Zaritsky, D., Donnerstein, R., Dey, A., et al. 2019, [ApJS](#), **240**, 1
- Zitrin, A., Acebron, A., Coe, D., et al. 2020, [ApJ](#), **903**, 137